



A manufacturing process for shaft and pipe couplings of Fe–Mn–Si–Ni–Cr shape memory alloys



A.V. Druker^{a,b,*}, A. Perotti^a, I. Esquivel^a, J. Malarría^{a,b}

^aFacultad de Cs. Ex., Ingeniería y Agrimensura (UNR), Av Pellegrini 250, 2000 Rosario, Argentina

^bInstituto de Física Rosario (CONICET-UNR), Bv. 27 de Febrero 210 bis, 2000 Rosario, Argentina

ARTICLE INFO

Article history:

Received 5 April 2013

Accepted 15 November 2013

Available online 25 November 2013

Keywords:

Shape-memory

Fe–Mn–Si

Formability

Welding

Manufacturing couplings

ABSTRACT

It has been shown that rolling an Fe–15Mn–5Si–9Cr–5Ni (wt.%) alloy at 800 °C followed by annealing at 650 °C gives a structure – a high density of stacking faults and enough austenite hardness – that promotes the stress induced martensitic transformation instead of plastic deformation. After this thermo-mechanical processing, the material recovers around 95% of a 3% permanent deformation excursion. This work addresses the formability and weldability of sheets processed in that manner and how welding affects the mechanical and shape memory properties. Here, the designs and verification are presented for a new method for manufacturing couplings by forming and welding, and finally, the degree of shape recovery in couplings manufactured by this new method are evaluated. The results show that these couplings recover 83% of their diametrical expansion, which make them suitable for many industrial applications.

© 2013 Elsevier Ltd. All rights reserved.

1. Introduction

Many polymers, ceramics and metallic alloys exhibit the shape memory effect (SME) [1]. In metals this behaviour is due to a stress-induced martensitic transformation that can be recovered when the material is heated. The Fe–Mn–Si based alloys have this property, and differ in some aspects from commercial steels [2]. The stable high-temperature austenitic phase (γ , FCC) transforms to a plate-like ϵ martensite (HCP) at room temperature. The SME takes place if the stress applied to induce the martensitic transformation does not produce plastic deformation, and if the $\epsilon \rightarrow \gamma$ reverse transformation occurs along the same crystallographic path followed during the direct transformation. The yield stress of the austenite as well as its microstructure and texture are among the parameters that affect the SME. Previous work has demonstrated that the favourable defect structure, a high density of stacking faults and a balance of dislocations, may be controlled by applying thermo-mechanical treatments to the material [3]. In particular, the combination of rolling at intermediate temperatures followed by annealing produces an almost perfect SME in Fe–Mn–Si alloys [4–6]. Druker et al. recently showed that rolling the Fe–15Mn–5Si–9Cr–5Ni (wt.%) alloy at 800 °C followed by annealing at 650 °C creates a structure – a high density of stacking faults and

enough austenite hardness – that promotes the stress induced martensitic transformation instead of plastic deformation. After this processing, the material recovers around 95% of a 3% permanent deformation excursion, making it suitable for practical applications [7].

Couplings for shafts and pipes are one of the more promising applications of these shape memory, ferrous-based alloys. Particularly when it is possible to replace traditional techniques that are difficult to apply in specific situations. Their advantages over the NiTi parts that are currently on the market are low cost, mechanical properties (strength, vibration mitigation and good creep rupture strength [8]) and technological characteristics (ductility, weldability, castability and workability [9]). The Japanese Nippon Steel Corp. has pioneered the developments. Later, Awaji Sangyo K. K. manufactured shape memory curved pipes and couplings to support civil structures [10–12]. The Shanghai Tianhe Shape Memory Materials Co., Ltd. offered pipe couplings and other products based on Fe–Mn–Si alloys containing rare earths [13]. Liu et al. mentioned the use of these alloys for petroleum and chemical industries [14]. More recently, Hiroshi et al. [15] presented centrifugal casted couplings for pipe joints in civil engineering constructions and established the limitations of shape recovery strain. Otsuka [1] and Dunne [16] summarize many others commercial applications and analysed successes and difficulties.

In general, the commercialization of couplings manufactured by centrifugal casting or forging did not succeed for two reasons. Firstly, the need of a training treatment increases the production costs. Secondly, it is very difficult to determine the final inner

* Corresponding author at: Facultad de Cs. Ex., Ingeniería y Agrimensura (UNR), Av Pellegrini 250, 2000 Rosario, Argentina. Tel.: +54 341 4808545; fax: +54 341 4218834.

E-mail address: ana@asb.com.ar (A.V. Druker).

diameter of the couplings at the end of the training process. As relatively high standard tolerances made impossible to ensure the maximum working pressure of the assembly, threaded couplings were tested [17].

The first prototype of welded couplings was developed by the National Institute for Materials Science in Japan. The coupling was prepared from a Fe–23Mn–6Si–5Cr–0.53Nb–0.06C (wt.%) alloy rolled at 600 °C and annealed to 300 °C for 10 min. The sheet was folded to 40 mm outer diameter and then welding by TIG method [18]. Some patents were based on this development [19–21], but are not yet commercially.

This work has four parts. Firstly, the formability and weldability are explored for a Fe–15Mn–5Si–9Cr–5Ni alloy rolled at 800 °C and annealed at 650 °C, and the effect of welding on the mechanical and shape memory properties is investigated. Secondly, the design and verification of a new method for manufacturing couplings by forming and welding is described. Then the degree of shape recovery is evaluated for the couplings manufactured by this new method, and finally, a theoretical analysis for the sizing of a power transmission coupling is presented.

2. Methods

The alloy was prepared by melting commercial-quality raw materials under an argon atmosphere in an induction furnace. Long, 10 mm thick ingots were obtained by casting into a sand mould. The ingots were homogenised at 1200 °C for 12 h and then rolled at 1000 °C to obtain sheets 1.7 mm in thickness. The sheet was given a final rolling reduction of 35% at 800 °C followed by a 650 °C anneal for 30 min. The composition of the alloy (as determined by chemical analysis) is indicated in Table 1.

The couplings were manufactured by plastic deformation using a specifically designed die and welded by the gas tungsten arc welded (GTAW) method. This was done with an ESAB Aristo Lud 450 welder, with a 2.4 mm diameter tungsten electrode held in a 10 mm diameter ceramic nozzle. An argon cover-gas atmosphere protected the coupling during welding.

Phase analysis was performed by XRD carried out in a Philips X-pert pro MPD goniometer using Cu $K\alpha_1/K\alpha_2$ radiation at 40 kV and 30 mA. The phase's hardness was evaluated by a Shimadzu microdurometer.

The microstructure was examined using optical microscopy (OM), transmission electron microscopy (TEM) and scanning electron microscopy (SEM). Specimens for optical and SEM observations were mechanically polished, finishing with 1200 grit emery paper. In order to remove residual stresses, the surfaces were electrolytically polished in a solution of 80% acetic + 20% perchloric acid at 27 V for 60–90 s. This procedure has the additional advantage of revealing the austenite grain boundaries. The examinations were performed using an Olympus PME3 optical microscope equipped with a Nomarski Interference Contrast (NIC) device, a Zeiss Axiolab, and a FEI Quanta 200 with Field Emission Gun, resolution of 10 nm and EBSD detector.

TEM specimens were chemically thinned to 0.2 mm using a solution of 90% H_2O_2 + 5% HF + 5% HNO_3 , and then electropolished with the double-jet technique in a 90% acetic + 10% perchloric acid solution at room temperature. Observations of the foils were made in a Phillips EM300 microscope operating at 100 kV.

Table 1
Alloy chemical composition (wt.%).

Fe	C	Mn	Si	Cr	Ni
65.31	0.05	15.43	5.50	8.10	5.61

Mechanical properties were evaluated by means of tensile tests performed using an Instron 3362 universal testing machine at a strain rate of $2 \times 10^{-4} \text{ s}^{-1}$. Shape memory properties were measured after 3% permanent uniaxial deformation, and after bending 90° around a 40 mm diameter mandrel. In this condition, the deformation in the outer fibre is $\varepsilon_b = t/\phi = 2.5\%$, where t is the sample thickness and ϕ , the mandrel diameter. Gauge dimensions of tensile and flat specimens were $3 \times 1 \times 60 \text{ mm}$ and $3 \times 1 \times 65 \text{ mm}$, respectively. The reverse transformation was activated by heating the samples at 550 °C for 20 min; this is well above the A_f temperature (see Table 2). The degree of uniaxial shape recovery (DSR_u) was determined as follows:

$$DSR_u = \frac{l_2 - l_1}{l_1 - l_0} \cdot 100, \quad (1)$$

where l_0 is the distance between two Vickers indentations measured before the tests, l_1 is the same length measured after the tensile deformation and l_2 is an equivalent measurement after recovery annealing.

The bent and flat sheet samples were photographed before and after annealing, and measured the angles: θ_e , elastic recovery, and θ_r after annealing. The degree of shape recovery, DSR_b , was calculated as:

$$DSR_b = \frac{90^\circ - \theta_r}{90^\circ - \theta_e} \cdot 100. \quad (2)$$

To evaluate the shape memory behaviour of the couplings, the diameter d was measured before and after the welded couplings had been expanded by a special device using the Instron machine (d_0 and d_1 , respectively), and after annealing (d_2). The degree of shape recovery of the couplings, DSR_c , was calculated as:

$$DSR_c = \frac{d_2 - d_1}{d_1 - d_0} \cdot 100. \quad (3)$$

3. Results and discussion

3.1. Material characterization

3.1.1. Mechanical properties of the rolled sheet

The sheets were prepared using the thermo-mechanical treatment that has shown the highest DSR [3]. It involves finish rolling at 800 °C and annealing at 650 °C for 30 min. Hardness was measured on specimens belonging to different sample batches. The interpretation of the hardness results must be well thought-out because material deformation occurs by both irrecoverable slip and a phase transformation. Thus, the results have to be considered only as tentative. Understanding this limitation and taking into account the samples thickness and the expected material hardness, the Vickers method was chosen. The average of 10 measurements gave a value of $HV_{0.3} 330\text{--}334$.

Samples for those tensile tests were prepared following the SAE J416 standard [22]. These results give data to design and calculate structures and mechanical parts. It can be seen from the curve in Fig. 1 that the material deforms elastically up to a stress of 350 MPa; permanent deformation begins at this point due to the $\gamma \rightarrow \varepsilon$ martensitic transformation and plastic slip. Young's modulus, as calculated by the Instron Bluehill2 program, is 123.6 GPa. After yield, the hardening rate decreases continuously until the ultimate strength of 880 MPa is reached, at which point the material fractures without necking. Total elongation, measured from the distance between the hardness indents, is nearly 16%.

Table 2
Transformation temperatures.

Sample	Ms	As	Af
Rolled at 800 °C and annealed at 650 °C for 30 min	−121.5	113.1	159
Rolled at 800 °C and annealed at 650 °C for 30 min plus annealed at 800 °C for 5 min	−82	123.5	151

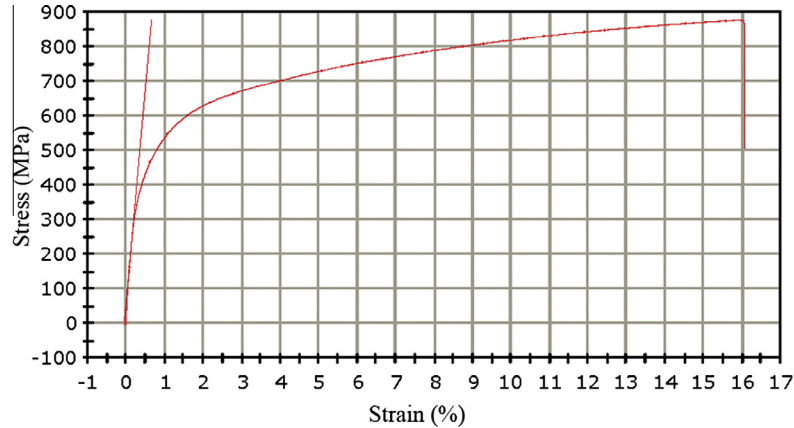


Fig. 1. Stress–strain curve obtained by tensile testing a sample taken from a sheet rolled at 800 °C and annealed at 650 °C.

3.1.2. Shape memory properties

The alloy chemical composition is crucial for good SM properties since the critical transformation temperatures – M_s and A_s – and the stacking fault energy depend on it. With the fabrication of shaft couplings in mind, it is desirable that the M_s is below room temperature and the A_s exceeds 50 °C. Simultaneously, to produce a good SME the stacking fault energy (SFE) should be as low as possible.

The four-probe resistivity method was used to measure critical temperatures of sheets rolled at 800 °C and annealed at 650 °C. Fig. 2 shows the measured curve (in black). The light curve corresponds to the same sheet after further heating at 800 °C for 5 min, which corresponds to the final condition of the couplings. The results are summarized in Table 2. In the last case, the hysteresis cycle is reduced, due to an increase in M_s temperature and a more sharp transition for the forward and reverse transformation. This indicates that annealing at 800 °C, even in a short time, reduces defects in the matrix and thus allows interfaces to move more easily than in the sheet annealed at 650 °C.

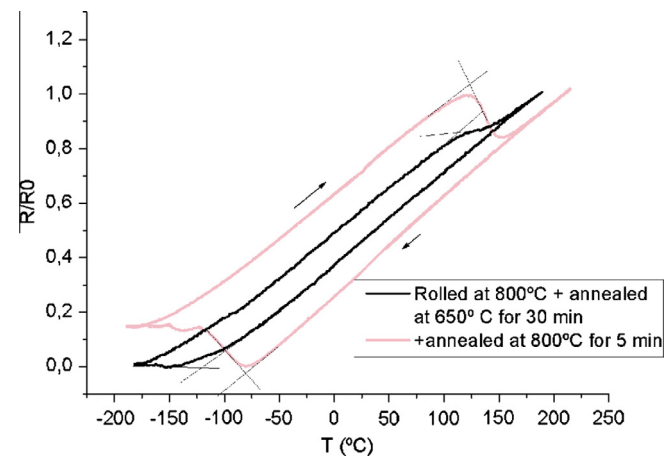


Fig. 2. Transformation temperatures of sheets treated in two different conditions.

On the other hand, the SFE can be estimated by the equation reported by Li et al. as function of chemical composition [23]:

$$\gamma_{\text{SFE}} \text{ (mJ/m}^2\text{)} = 28.87 + 0.21x\% \text{Mn} - 4.45x\% \text{Si} - 1.1x\% \text{Cr} + 1.64x\% \text{Ni}$$

The calculated value, 7.926 mJ/m², is actually very low as desired to promote good SM properties [23].

Additional samples for tensile and bend tests were prepared in the manner described above, in order to confirm the material's previously reported shape memory behaviour. The following values were found:

$$DSR_u = 95\% \text{ and } DSR_b = 98\%.$$

The stress that induces the martensitic transformation, $\sigma_{\gamma \rightarrow \epsilon}$, was 350 MPa. The reader should also note that the bending test values are somewhat higher due to the strain gradient in these samples' test section. These results illustrate the reliability of the tests that were performed, and show that this alloy has the repeatability of shape memory behaviour required for a commercial product.

On the other hand, it is important to compare the SM behaviour of the material in the rolled condition to material obtained by casting or forging. Li et al. [9] prepared specimens for bending experiments by cutting plates from cast (after a solution treatment) and forged pipes of a similar alloy. The specimens were bent 180° around steel rods and then recovered at 600 °C for 30 min. The DSR_b , measured for a 2% prestrain, were 87.5% and 89% for the cast and forged alloys, respectively. The microstructure of rolled sheets has been shown to be most appropriate for the introduction of fine plates of ϵ martensite, providing an almost complete retransformation.

3.1.3. Weldability

Based on previous welding studies using these kinds of alloys [24,25], the GTAW process was applied to manufacture the welded pipes. This high-energy-density method is appropriate for small sheet thicknesses.

A first step in assessing a material's weldability is to determine "the capacity of a material to be welded under the imposed fabrication conditions into a specific, suitably designed structure and to perform satisfactorily in the intended service" [26]. So, many tests were

performed to estimate the effects of welding on the cracking and ductility of both base and weld-metal, the weld penetration, the weld-pool shape and fluid flow and, not the least important, the SME.

Sheets 1 and 2 mm thick were rolled at 800 °C and then butt welded with the GTAW method, without filler metal. Table 3 summarizes the process parameters.

After cutting by electrical discharge machining (EDM), samples belonging to these three batches were annealed at 650 °C. Visual inspection and macro-examination showed no defects in the face or root of the seams, as can be seen in Fig. 3. Sectioning the weld beads also revealed no internal defects, and good weld penetration and fusion. During the tensile tests, rupture (brittle fracture) occurred in the weld beads – as can be seen in Fig. 4 – after reaching maximum stresses of about 650 MPa.

3.1.4. Effect of welding on microstructures

Microstructural analysis of the welded zone, shows a cellular–dendritic structure, due to solidification after welding, as can be seen in Fig. 5. This NIC micrograph taken from an electropolished sample clearly allows the reader to appreciate the columnar dendritic growth mode. Such a structure indicates that the temperature gradient was relatively low and the degree of constitutional supercooling was great, which allows for larger protrusions and the development of cellular and columnar dendritic growth [27]. The microstructure is described in detail below.

Fig. 6 shows OM observations of the welded-sheet microstructure. It is easy to recognize three zones: the welded zone (WZ), the heat-affected zone (HAZ) and the base-metal (BM). XR patterns of the BM (Fig. 7a) shows the predominant presence of austenite and low-intensity peaks corresponding to a second phase. Both phases are recognizable in the high-magnification image shown in Fig. 8. Microhardness values taken from each phase are significantly different: $HV_{0.025}$ 967–1050 for the precipitate and $HV_{0.025}$ 302–325 for austenite. The quantity of second phase was estimated at $7 \pm 1\%$, using the KS1003.0 program for image analysis available on the Zeiss microscope. TEM images presented in Fig. 9 show the precipitates, isolated dislocations and a high density of stacking faults in the austenite. According to the X-ray diffraction analysis, these peaks could be characteristic of the $Fe_5Ni_3Si_2$ precipitate. However previous findings reported in the literature [28–33] show that different intermetallic phases or carbides can precipitate in this kind of alloys. The complete analysis of the microstructure and phases present in the material will be published in a subsequent article devoted to the specific topic.

XR only detected austenite in the zones affected by the welding (Fig. 7b). Recrystallized grains in the HAZ have grown to about 300 μm , as the SEM image in Fig. 10 shows. Ferrite almost disappeared from the material indicating that the temperature reached a range between 1000 and 1100 °C. Maji et al. [29] have shown that in these kinds of alloys only austenite is stable within this range. Fig. 11 shows that stacking faults are stopped by the grain boundaries. Plates of ϵ martensite plates crossing the boundaries are also observed. Thermal martensite is another consequence of grain growth, which increases the Ms. above ambient temperature [34].

The austenitic cellular–dendritic structure in the WZ contains a low-density distribution of defects, as can be observed in Figs. 12 and 13, corresponding to OM and TEM images, respectively.

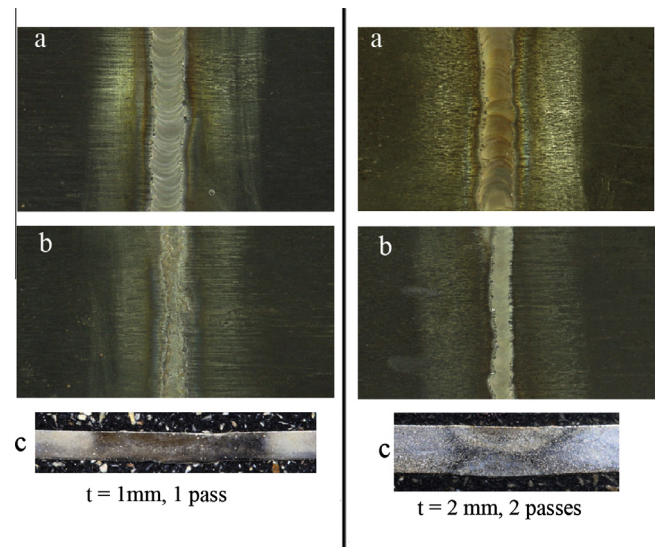


Fig. 3. Macro-examination of the welded seams: (a) face; (b) root; (c) cross section. Thicknesses and number of passes are explained.

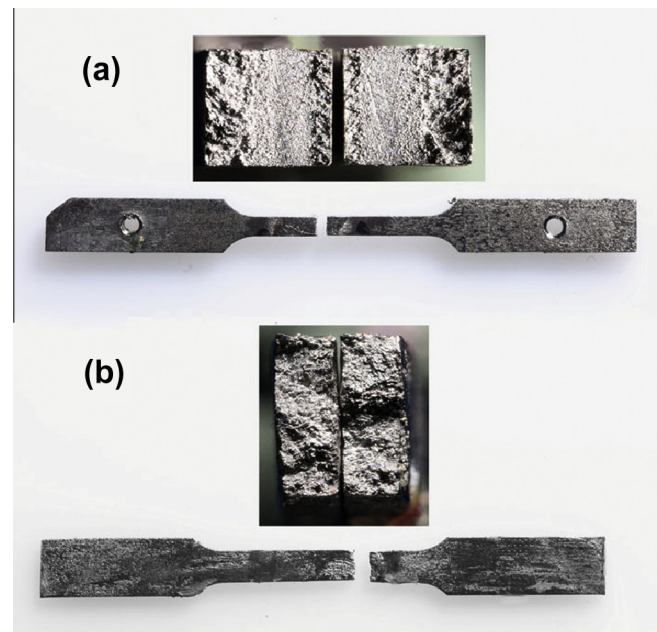


Fig. 4. Samples of different thicknesses showing brittle fracture in the welded zone (a) $t = 2$ mm; (b) $t = 1$ mm.

The absence of dislocations in the austenitic matrix and the grain growth in the HAZ and the WZ, could degrade the shape memory properties. On the other hand, Lin et al. [24] have reported a reduction of the Mn content in the TIG welded zones in a Fe–30Mn–6Si specimen. This reduction has been attributed to Mn vaporization during welding, and the authors suppose that the Mn depletion has a significant influence on the shape memory effect.

Table 3
GTAW process parameters.

Sample thickness	Current (A)	Voltage (V)	Average power (kW)	Slope up (s)	Slope down (s)	Pre-flow (s)	Post-flow (s)	Gas flow rates (ft ³ /h)
1 mm	28	12.3	0.36	1.6	1.6	2.2	3	18
2 mm (face)	42	12.7	0.52	1.6	1.6	2.2	3	18
2 mm (face and root)	28	14.2	0.4	1.6	1.6	2.2	3	18

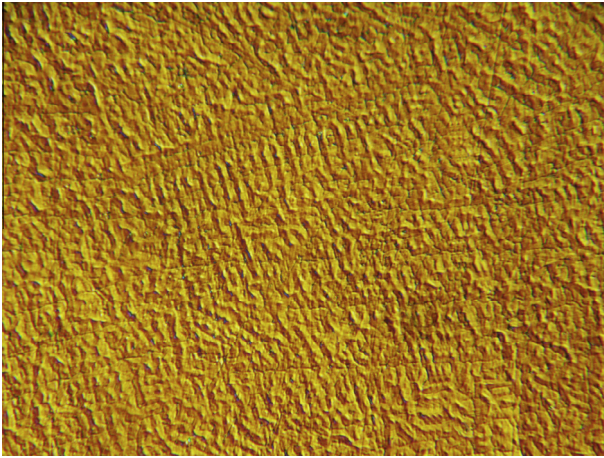


Fig. 5. Micrograph of the welded zone showing a columnar dendritic growth structure.

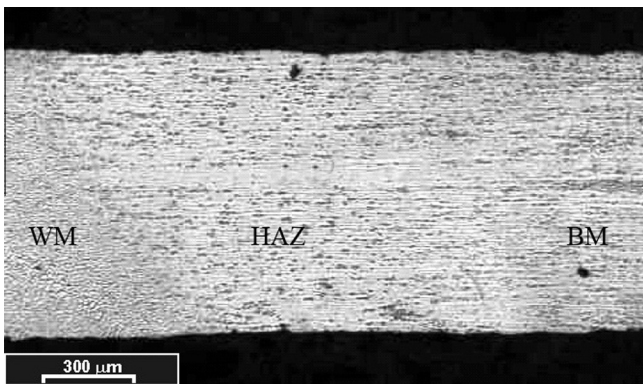


Fig. 6. OM image of the microstructure of the welded sheet: welded zone (WZ), heat affected zone (HAZ), base metal (BM).

Microstructural observations do not support this scenario. If the Mn content decreases the relative Cr content would increase and, with it, the possibility of stabilizing ferrite at room temperature. Because this did not happen, the Mn content does not seem to have been reduced.

To evaluate the effect of welding on the shape memory behaviour, one batch of tensile samples was deformed to 3% permanent elongation, and bending tests were performed on another batch. After inducing the reverse martensitic transformation by heating to 550 °C, the results were as follows:

$$DSR_u = 50\% \quad DSR_b = 87\%,$$

which indicates that the effect of welding depends on the load application mode. The deterioration of the shape memory behaviour is less than 15% in flexure, but is very significant after tensile–stress deformation. This may be ascribed to the formation of dendrite structures. That is, the dendrite structures in the welded zones will slightly degrade the specimen's shape memory effect. Lin et al. [24] reported a $\pm 10\%$ variation of shape memory effects due to welding.

3.1.5. Formability

From the beginning, the intent was to manufacture coupling prototypes by plastic deformation of the rolled sheet. Thus, it was necessary to study the material formability that is the ease with which the alloy can be shaped during sheet-forming operations [35]. Formability indices provide quantitative estimates of

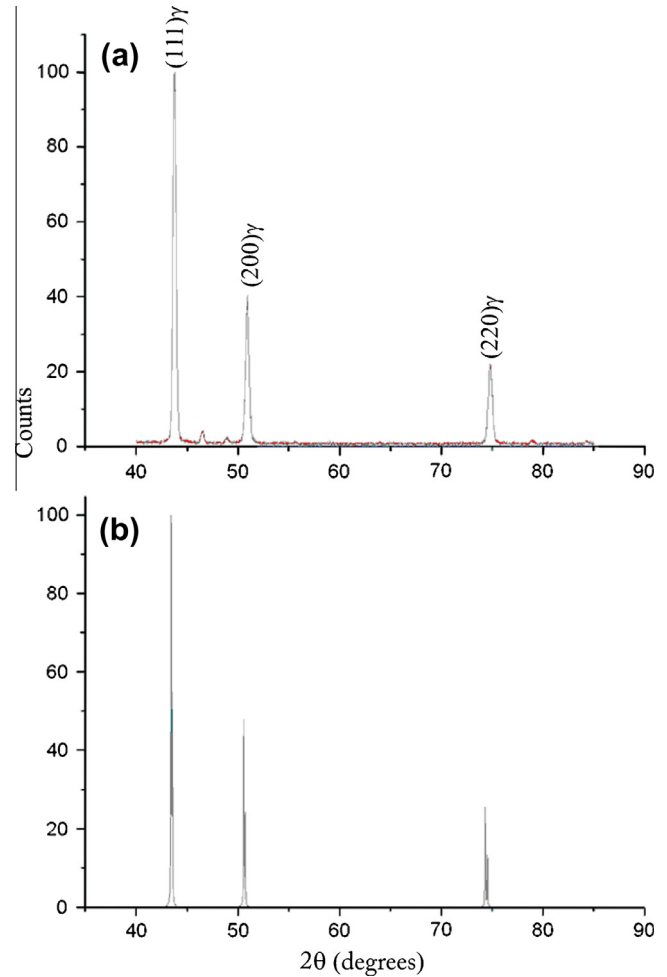


Fig. 7. XR patterns measured from (a) base metal and (b) heat affected zones.

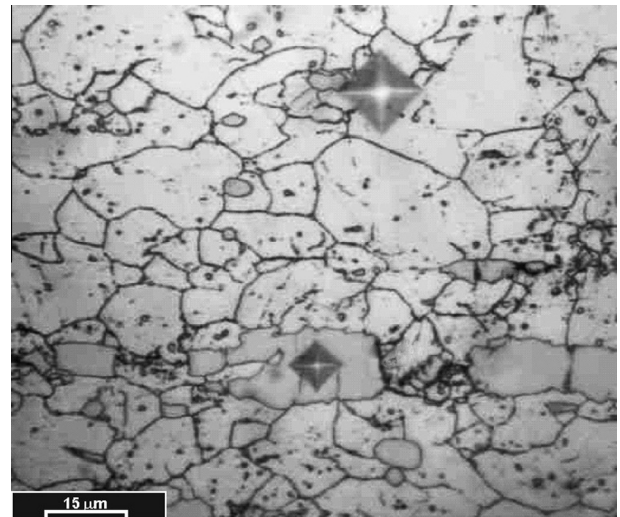


Fig. 8. Microstructure of the BM; indentations show the hardness difference between ferrite (bright grains) and austenite.

the strength properties of a metal (and therefore the required working loads) and its resistance to failure. The required mechanical properties include those determined by tension testing and by

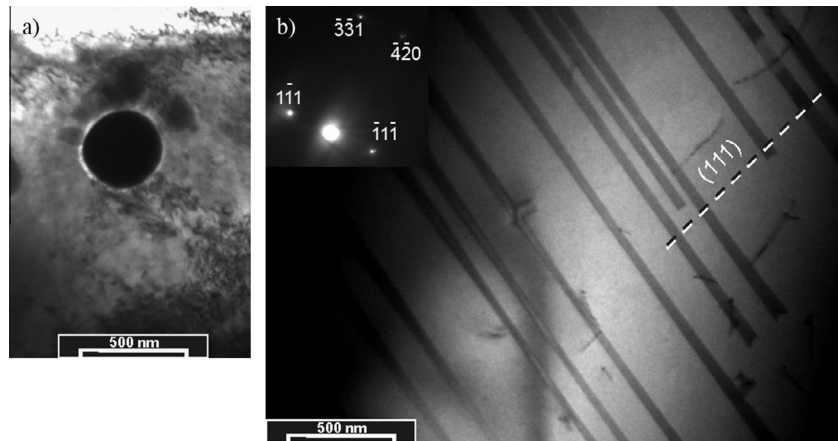


Fig. 9. TEM images from the BM showing a small quantity of precipitates, isolated dislocations and a high density of stacking faults in the austenite.

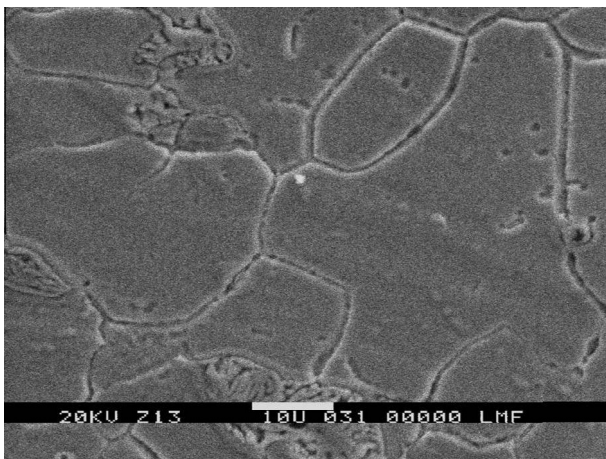


Fig. 10. SEM image from the HAZ showing that recrystallized grains have grown to about 300 μm .

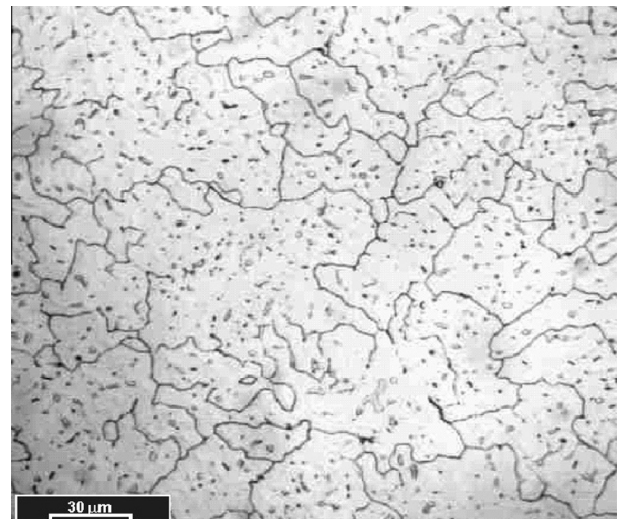


Fig. 12. OM image of the structure resulting from solidification in the WZ.

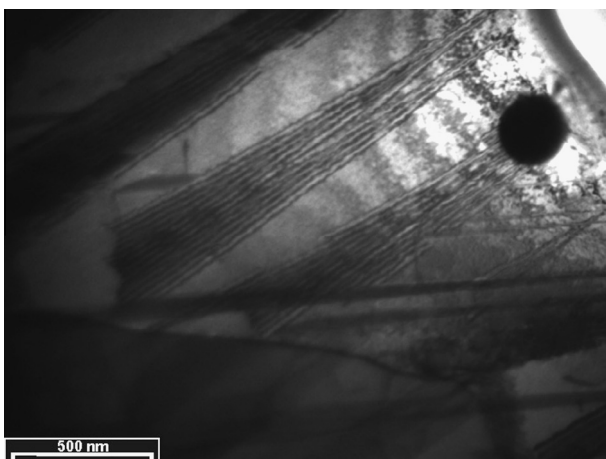


Fig. 11. TEM image from the HAZ showing that stacking faults are stopped by the grain boundaries.

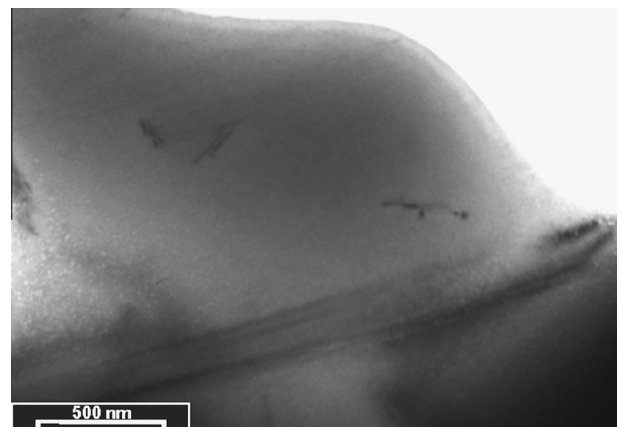


Fig. 13. TEM image from the WZ showing a low density distribution of defects.

other tests designed to simulate various production forming processes, including cup tests and bend tests.

Bending is the most common type of deformation, and surely it will occur in the current manufacturing process. Following the literature, the major problems we could encounter in forming this

alloy are fracture, buckling and wrinkling, shape distortion, loose metal and undesirable surface textures. The occurrence of any one or a combination of these conditions can render the material unusable. So, intrinsic formability tests were developed to measure the characteristic properties of materials that can be related to

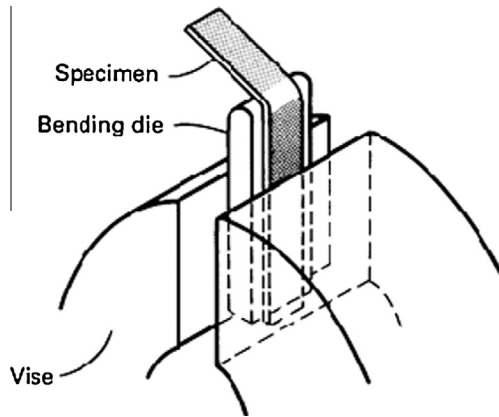


Fig. 14. Schematic of the simple bend test [35].

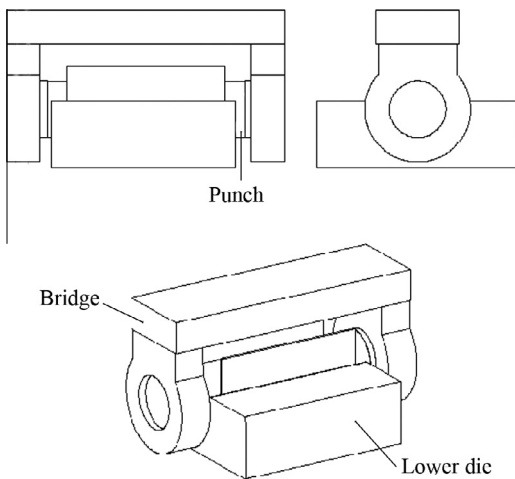


Fig. 15. Assembly plane of the compound bending die.

their formability. The results are insensitive to the thickness and surface condition of the material. The most important and extensively used intrinsic test is the uniaxial tensile test, which provides the values of many material properties for a wide range of forming operations. The results obtained from samples subjected to tensile tests are shown above.

Among other commercially important intrinsic experiments, the *simple bend test* is useful in predicting the alloy's performance when bent without tension. The simplest method for bending thin sheet material is to clamp a specimen and a bending die in a vise, as shown in Fig. 14, and then to bend the specimen over the die manually or with a nonmetallic mallet.

Using fixturing like that shown in Fig. 14, a sample from a rolled and annealed sheet was prepared and manually bent 180° around a 40 mm diameter die. The material deformation in the outer fibre of the sheet was 2.5%. No damage appeared after bending. That is, no evidence of fracture or surface irregularities were found.

In order to investigate the martensitic transformation that had occurred during this formability test and the accompanying shape memory behaviour, the sample was heated to 550 °C to activate the reverse transformation. The sample recovered 157° of the original 180° of bending deformation. This translates to 87% shape recovery.

Thinking about the SME of the finished part, this result represents a high percentage of deformation recovery. However, if bending occurs during the fabrication of a part, it could present a significant problem.

3.2. Manufacture of coupling prototypes

3.2.1. Die design

To manufacture the first prototypes from shape memory sheets, a device on the laboratory scale was designed and used in a manually operated hydraulic press. Fig. 15 shows the assembly plane of the compound bending die.

The fabrication fixture has four parts: upper and lower dies, a punch, and a bridge. In order to select the most appropriate steel



Fig. 16. The images show three stages during the forming operation.

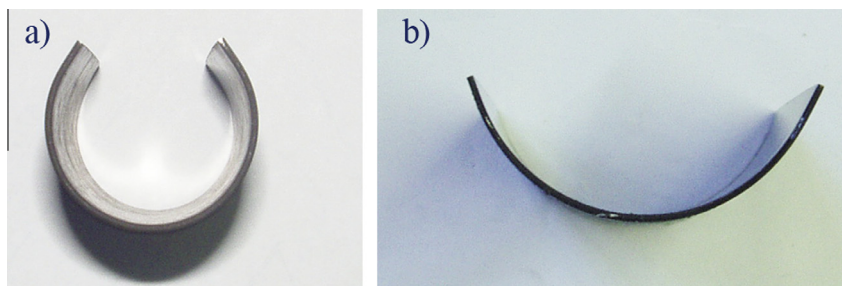


Fig. 17. (a) Elastic recovery and (b) shape memory recovery, shown during manufacturing.



Fig. 18. Redesigned bending die; the stud bolts will be adjusted with wing nuts to maintain the pressure during heating.

for these tools, it should be considered that wear determines the useful performance of a press forming die. In general, total wear is primarily affected by the length of the production run and the severity of the forming operation. This total wear may be produced by abrasion or adhesion (galling), or both [35]. Taking into account the alloy hardness and a short production run, a 0.45% plain carbon steel was selected for the die parts and punch. The parts were machined and then quenched and tempered to HRC 48, which is common manufacturing tool hardness. The bridge was built of 0.10% plain carbon steel.

The sheet was deformed in successive stages in the lower die, bending the sample around the punch, which was horizontally supported by the bridge. Then, the bridge was replaced by the upper die, which closes the sheet into a ring. Fig. 16 illustrates three stages that occurred during the forming operation.

After the first sheet-forming attempt, the material recovered elastically, when the dies were opened and the punch removed. This can be seen in Fig. 17a. Moreover, upon heating to 550 °C –

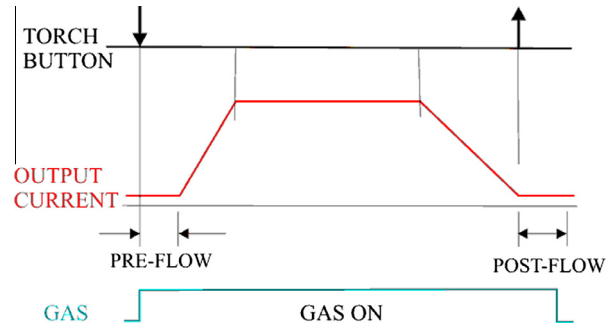


Fig. 20. Process operating sequence used for weld couplings.

above the reverse transformation temperature – the sheet partially recovered its flat shape (Fig. 17b).

Thus, the shape memory effect can play an unexpected role during manufacturing. During welding, if the material attempts to recovery its shape, high stresses may be produced in the seams, leading to fracture of the welded tube. The fabrication process must guarantee that the sheet only deforms plastically and no recoverable deformation is produced.

To eliminate elastic spring back and shape-memory recovery during annealing, a new die design was created. The new design is simple as only threaded holes were added to accommodate stud bolts adjusted with wing nuts, see Fig. 18. Using this modified fixture, the second test was performed.

After completely deforming the sheet into a tube, the wing nuts were adjusted to fix the upper and lower press dies in place. Then, this closed assembled set – the sheet, punch, and upper and lower dies – was heated in a furnace to 550 °C. When the shape memory material was heated above the reverse transformation temperature, the closed die/punch system prevented shape recovery. The stress developed within the fixture during annealing plastically deforms the austenite because the alloy is above the M_d temperature.

3.2.2. Welding

In addition, it was necessary to design a device to hold the tube for welding. Again, a closed shape was selected – with a slot through which we could run the weld bead – in order to prevent deformation during processing. This fixture is shown in Fig. 19.

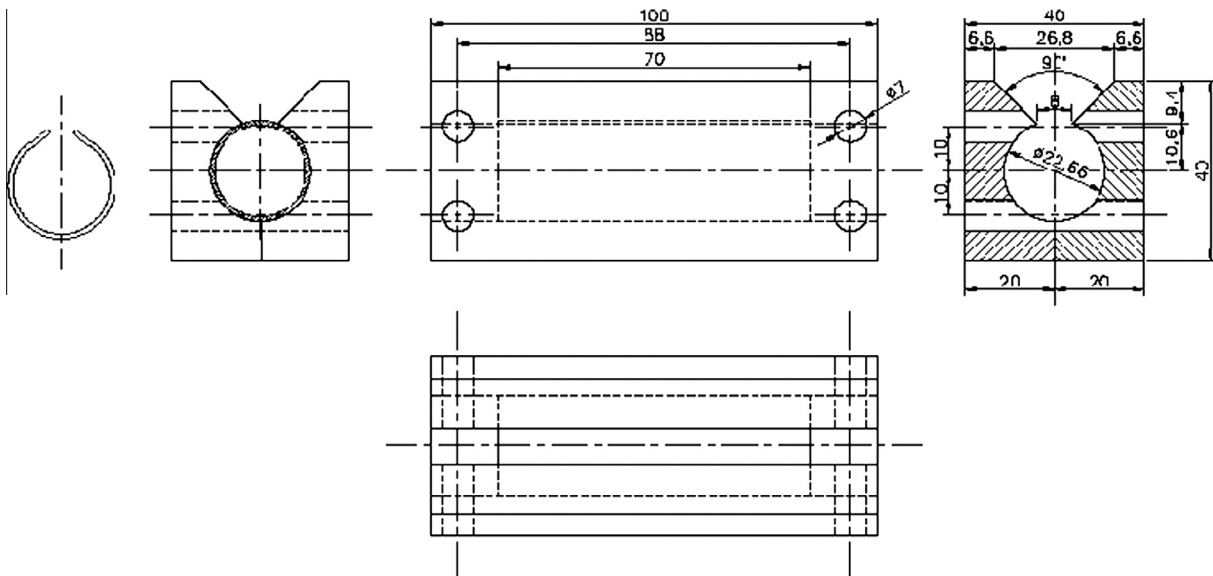


Fig. 19. Design of a device to hold the tube for welding.



Fig. 21. Photograph of a prototype coupling.

Fig. 20 shows the process operating sequence, and the welding conditions follow:

- Direct current electrode negative: 28 A.
- Argon Flow Rates: 8.4 L/min (18 CFH).
- Gas pre-flow: 2.2 s.
- Gas post-flow: 3 s.
- Slope up time: 1.6 s.
- Slope down time: 3 s.

Fig. 21 shows the finished prototype coupling.

3.3. Degree of shape recovery and torsional resistance

To determine the shape memory behaviour, the couplings need to be expanded circumferentially. This was done with an elastic sleeve and punch set made from SAE 1541 steel [36] quenched and tempered to HRC 48. Fig. 22a is the shop drawing of the elastic sleeve and the punch, and Fig. 22b shows the finished parts. The

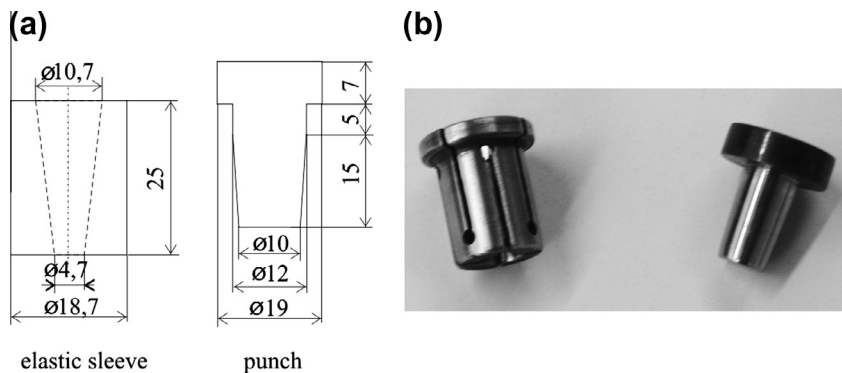


Fig. 22. Ring expansion tools: (a) shop drawing of the elastic sleeve and the punch to expand the couplings, (b) the finished parts.

Table 4
Degree of shape recovery of couplings annealed at different temperatures.

	d_0 (mm)	d_e (mm)	P (N)	d_f (mm)	ER (%)	d_2 (mm)	ε (%)	DSR (%)
Annealed at 650 °C, 30 min	22.03	22.90	4000	22.70	0.9	22.17	3.0	79
Annealed at 800 °C, 30 min	21.82	22.78	5300	22.61	0.77	21.95	3.6	83
Annealed at 1000 °C, 30 min	22.38	23.18	6500	23.13	0.22	22.77	3.35	48

Where P is the applied load (N), ER the amount of elastic recovery (%), ε the permanent deformation (%) and DSR is the degree of shape recovery (%).

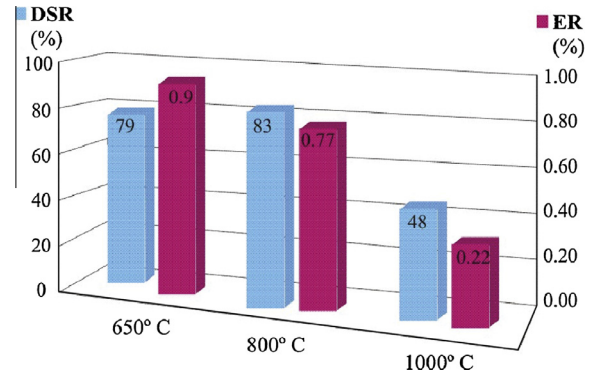


Fig. 23. Graphs show the results of the shape memory tests of the couplings. DSR: degree of shape recovery. ER: elastic recovery.

tubes were expanded by applying a compressive load in the Instron 3362 testing machine.

Three batches of samples, annealed at different temperatures after welding, were prepared. The outer diameter was measured before expansion (d_0), during expansion (d_e), after elastic recovery (d_f), and after heating for shape recovery (d_2). Table 4 shows the results, which are also graphed in Fig. 23.

The results show that the couplings manufactured in the manner explained above and annealed at intermediate temperatures have very good shape memory behaviour. On the other hand, annealing at 1000 °C degrades the properties and softens the austenitic matrix. The degree of shape recovery by the couplings annealed at 650 °C was 13% lower than that of the sheets. This could be due to stresses accumulated in the material as a consequence of welding, which remain even after the heat treatment. Annealing at 800 °C seems to improve shape recovery. A recovery of 83% of the permanent deformation was obtained with this anneal, which is enough for many industrial applications.

After obtaining these results, a special test was prepared to assess the performance of in-service couplings. Previously expanded samples were positioned (with minimum slippage) to transmit torque from one shaft to another. The assembly was heated at 500 °C

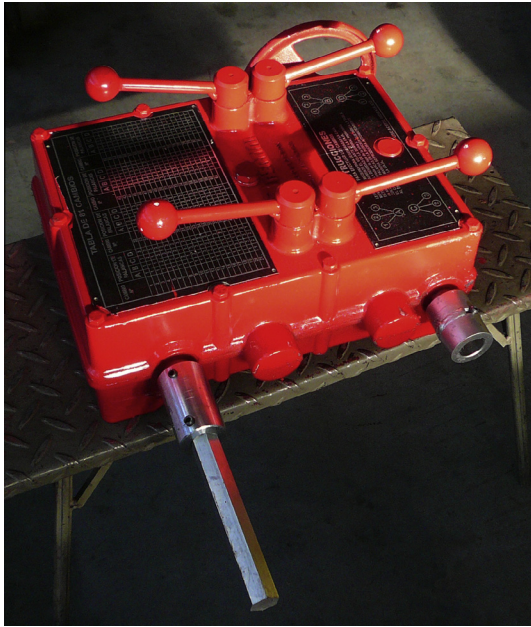


Fig. 24. Location of the coupling on the kinematic control train for a farm implement.

for 20 min. to activate the reverse martensitic transformation and to generate stresses as a result of the prohibited shape recovery. We used a torque meter to measure the coupling's resistance to torsional slippage in prototypes of internal contact area of 5.6 cm^2 . The value indicated by the gage was 6 kgm which means that the system supported 170 MPa of shear stress, assuming a coefficient of friction of 0.1. This is an anticipated value, taking into account that the coupling is only 1 mm thick. Kajiwara et al. [18] showed a welded coupling made from 2 mm thick plates of a Fe–28Mn–6Si–5Cr–0.5NbC alloy, although no torsional test results are given in their work.

4. Sizing of a power transmission coupling

The following analysis will show how the couplings might be applied to the special case of a junction to transmit power between aligned, 0.1% C carbon steel bars. The bars and coupling are part of the kinematic control train for a farm implement. Currently, these machines have movable joining systems that are connected and fixed using bolts, spikes and wedges (Fig. 24). Besides being more expensive, there is risk of excessive clearance, wear and joint malfunction. Heat-shrink couplings were rejected by the manufacturer due to the proximity of the joint with the gearbox, which is already finished at the time of assembly. Thus, this gear case would be affected during the installation of the hot coupling. The SM coupling is easily positioned at room temperature, and then a heating element is carefully placed on the coupling to activate the reverse transformation to austenite, reducing the internal diameter. The advantage of the SM alloy over other options – the heat shrink coupling or welding – lies in its simplicity and ease of assembly. The bars are cold-drawn rods $\text{Ø}22$. The couplings' as manufactured inner diameter, d_0 , must be such that once they are expanded to d_1 , the components can not only be assembled easily but they must have a close dimensional fit. Following the ISO and ASME Standards [37,38] and accounting for results obtained from previous tests on prototypes, the interference between bars and couplings – after the couplings have been heated to activate the reverse transformation was calculated. Appendix A shows the calculations,

which were based on a standard tolerance for bars and the eventual manufacturing variability. The resulting interference values vary between 0.3 and 0.5 mm. These values exceed the recommendations given for transmission of high torques, when comparing SM couplings to an alternative shrink-fit assembly method. Later it will be necessary to iteratively fit actual part dimensions (including the couplings' thickness) to achieve the desired torque transmission.

5. Conclusions

This work addressed the mechanical, technological and recovery properties of shape memory ferrous couplings. The conclusions are the following:

1. Sheets of a Fe–15Mn–5Si–9Cr–5Ni alloy rolled at 800 °C and annealed at 650 °C have appropriate formability and weldability
2. Welding affects mechanical and shape memory properties. The material fractured in the welded zone, and the degree of shape recovery decreased 15%, as measured with flexure tests. The decrease in shape recovery is also significant in tensile tests, but the affected zone is small.
3. A new method to manufacture couplings by forming and welding was presented and proved to be successful.
4. The degree of shape recovery of the couplings manufactured by this new method depends on the annealing temperature after welding. The couplings annealed at 800 °C recovered 83% of the 3.6% permanent diametrical expansion.
5. The sizing of a power transmission coupling has shown that this method can develop sufficient coupling force.

The results of this investigation are promising, and they encourage continued working.

Acknowledgements

The authors acknowledge financial support from ANPCyT (PICT 1128), SecTyl-Prov. Santa Fe (2010-156-11) and SCyT-U.N.R. (PID ING255).

Appendix A

A.1. Assembly conditions

The rods to be connect are commercial cold-drawn bars $\text{Ø}22\text{h}11$ (that is $\text{Ø}22_{-0.1230}^{+0}$) = d_b . To facilitate assembly and yet obtain a close dimensional fit, an expanded coupling size (inner diameter after expansion to induce the martensitic transformation) of $d_1 = \text{Ø}22\text{D}12 \text{ Ø}22_{+0.065}^{-0.275}$) was adopted. The greatest tolerance is due to variability in the coupling expansion operation. After this deformation, the maximum and minimum locational clearances are 0.405 and 0.065 mm, respectively. Most likely, a clearance of about 0.170 mm can be expected, which is more than sufficient for smooth assembly.

A.2. Sizing the coupling's manufacturing dimensions

A 3.6% permanent deformation was applied to the prototype couplings to induce the martensitic transformation, so this value will be adopted for the calculations. In this case, the inner coupling manufacturing dimension must be: $d_0 = 21,3_{+0.05}^{+0.13}$ mm

Verifying : $d_0 \text{max.} + 3.6\% \text{ max. permanent deformation} = 22.20 \text{ mm}$
 $d_0 \text{min.} + 3.6\% \text{ min. permanent deformation} = 22.12 \text{ mm}$

It can be seen that the calculated values fall within the allowable range for d_1 . The resulting tolerance is necessary due to the expansion inaccuracies, mentioned above.

A.3. Capacity for power transmission after shape recovery

An 83% shape recovery (DSR) was measured on the prototype couplings. Thus, the final outer diameter, considering tolerances, would be:

$$DSR = \frac{d_1 - d_2}{d_1 - d_0} \times 100 \rightarrow d_2 = d_1 - \left(\frac{d_1 - d_0}{100} \times DSR \right) \quad (A1)$$

$$d_{2 \max.} = d_{1 \max.} - (d_{1 \max.} - d_{0 \max.}) \times 0.83 \\ = 22.275 - (22.275 - 21.430) \times 0.83 = 21.574 \text{ mm}$$

$$d_{2 \min.} = d_{1 \min.} - (d_{1 \min.} - d_{0 \min.}) \times 0.83 \\ = 22.065 - (22.065 - 21.350) \times 0.83 = 21.472 \text{ mm}$$

If the coupling experiences the reverse transformation mounted over the cold-drawn $\varnothing 22 \text{ h}11 = d_b$ bar, the theoretical interference (γ) will be:

$$\gamma_{\max.} = d_b \max. - d_{2 \min.} = 22 - 21.472 = 0.528 \text{ mm}$$

$$\gamma_{\min.} = d_b \min. - d_{2 \max.} = 21.870 - 21.574 = 0.296 \text{ mm}$$

In the case of a shrink-fit coupling, the norm recommends an interference of $0.001 \times D$ (mm) – in the current case 0.022 mm – for high torque transmission. Thus, these calculations demonstrate that it is possible to develop a sufficient coupling force.

On the other hand, the system must keep working conditions below the yield strength of both materials. There is a relationship between the interference and the pressure generated at the bar/coupling contact surface:

$$p = \frac{\delta}{2b \left[\frac{1}{E_c} \left(\frac{c^2 + b^2}{c^2 - b^2} + \nu_c \right) - \frac{\nu_b}{E_b} \right]}, \quad (A2)$$

where E is the Young's modulus; ν the Poisson's ratio; δ the diametrical interference; $b = d_b/2$; and c is the coupling outer diameter/2.

The corresponding values are $E_b = 200$ GPa, $E_c = 123.58$ GPa, $\nu \cong 0.3$, $b = 11$ mm, $c = 12$ mm.

The amount of interference must also be sized to meet a maximum pressure condition. This pressure was calculated according to the alloy's mechanical properties (see Fig. 1) and the assumption that the couplings act as small thin-walled cylinders. Thus,

$$\sigma_t = p \times \left(\frac{b}{c - b} \right) \geq \sigma_{\text{adm.}} \quad (A3)$$

As a worst case condition, consider $\sigma = 350$ MPa, which gives a maximum pressure of 31.8 MPa. Using this value in Eq. (A2), a maximum interference can be calculated.

The final coupling design is determined by these two interference limits. Manufacturing diameter and wall thickness are parameters that will vary, dependent on each specific case.

References

- [1] Otsuka K, Wayman CM. Shape memory materials. New York: Cambridge University Press; 1998.
- [2] Sato A, Chishima E, Soma K, Mori T. Shape memory effect in $\gamma \leftrightarrow \epsilon$ transformation in Fe-30Mn-1Si alloy single crystals. *Acta Metall* 1982;30:1177–83.
- [3] Druker A, Baruj A, Malarría J. Effect of rolling conditions on the structure and shape memory properties of Fe–Mn–Si alloys. *Mater Charact* 2010;61:603–12.
- [4] Stanford N, Dunne D, Li H. Re-examination of the effect of NbC precipitation on shape memory in Fe–Mn–Si-based alloys. *Scr Mater* 2008;58:583–6.
- [5] Söderberg O, Liu X, Yakovenko P, Ullako K, Lindroos V. Corrosion behaviour of Fe–Mn–Si based shape memory steels trained by cold rolling. *Mater Sci Eng, A* 1999;273–275:543–8.
- [6] Baruj A, Troiani H. The effect of pre-rolling Fe–Mn–Si-based shape memory alloys: mechanical properties and transmission electron microscopy examination. *Mater Sci Eng, A* 2008;481:574–7.
- [7] Druker A, Perotti A, Baruj A, Malarría J. Heat treatments of Fe–Mn–Si based alloys: mechanical properties and related shape memory phenomena. *J. ASTM Int* 2011;8(4):1–8.
- [8] Takahiro S, Puspendu S, Takehiko K, Kazuyuki O, Setsuo K, Atsumichi K, et al. Vibration mitigation by the reversible fcc/hcp martensitic transformation during cyclic tension – compression loading of an Fe–Mn–Si-based shape memory alloy. *Scr Mater* 2006;54:1885–90.
- [9] Li JC, Zhao M, Jiang Q. Comparison of shape memory effect between casting and forged alloys of Fe14Mn6Si9Cr5Ni. *JMEPEG* 2002;11:313–6.
- [10] Awaji M. Characteristics and applications of Fe–Mn–Si-based shape memory alloys, Technical report 2008 <http://www.awaji-m.jp/english/r_and_d/pdf/memory_alloy.pdf>.
- [11] Maruyama T, Kurit T, Kozaki S, Andou K, Farjami S, Kubo H. Innovation in producing crane rail fishplate using Fe–Mn–Si–Cr based shape memory alloy. *Mater Sci Tech Ser* 2008;24:908–12.
- [12] Maruyama T, Tanahashi H, Asai Y, Mio T. Patent JP5215277, Pub.: 24/8/1993 (Japan).
- [13] Liu W, Liu D, Gong F, Wang D; Patent WO9935298 (International) and related, Pub.: 15/7/1999.
- [14] Liu DZ, Wang DF, Ji WY, Liu WX. In: Proc. 2nd Int. Conf. on Shape Memory and Superelastic Technologies, SMST 1997, California; 1997. p. 329–34.
- [15] Hiroshi K, Otsuka H, Farjami S, Maruyama T. Characteristics of Fe–Mn–Si–Cr shape memory alloys in centrifugal casting. *Scripta Mater* 2006;55:1059–62.
- [16] Dunne D. Shape memory in steels, in phase transformations in steels. Woodhead Publishing 2012;2:83–125.
- [17] Tanahashi H, Maruyama T, Kubo H. Applications of Fe–Mn–Si alloy for pipe joints. *J Adv Mater* 93, V/B: Shape Memory Mater Hydrides, *Trans Mat Res Soc Jpn* 1994;18B:1149–54.
- [18] Kajiwarra S, Baruj A, Kikuchi T, Shinya N. Low-cost high-quality Fe-based shape memory alloys suitable for pipe joints. In: Proc. SPIE 2003, smart structures and materials 2003: active materials: behaviour and mechanics; 5053:250–261. doi:10.1117/12.484341.
- [19] Kikuchi T, Kajiwarra S, Baruj A, Ogawa K, Shinya N. Working and heat-treating method for Fe–Mn–Si based shape memory alloy added with NbC. Patent JP2003105438. Pub.: 9/4/2003.
- [20] Kikuchi T, Kajiwarra S, Baruj A, Ogawa K, Shinya N. Method of processing and heat-treating NbC-added Fe–Mn–Si-based shape memory alloy. Patent EP20030251736 (EU) and related, Pub.: 1/10/2003.
- [21] Kikuchi T, Kajiwarra S, Baruj A, Ogawa K, Shinya N. Method of thermo-mechanical-treatment for Fe–Mn–Si shape-memory alloy doped with NbC. Patent WO2004055222 (International) and related, Pub.: 1/7/2004.
- [22] Tensile test specimens–SAE J416 DEC83. SAE Handbook 1995; 1:3.01. Society of Automotive Engineers. Warrendale, U.S.A.
- [23] Li JC, Zhao M, Jiang Q. Alloy design of FeMnSiCrNi shape-memory alloys related to stacking-fault energy. *Metall Mater Trans A* 2000;31:581–4.
- [24] Lin HC, Lin KM, Chuang YC, Chou TS. The welding characteristics of Fe–30Mn–6Si and Fe–30Mn–6Si–5Cr shape memory alloys. *J Alloys Compd* 2000;306:186–92.
- [25] Donga ZZ, Sawaguchi T, Kajiwarra S, Kikuchi T, Kimb SH, Lee GC. Microstructure change and shape memory characteristics in welded Fe–28Mn–6Si–5Cr–0.53Nb–0.06C alloy. *Mater Sci Eng, A* 2006;438–440:800–3.
- [26] Standard Welding Terms and Definitions. *Ansi/Aws A3.0-89*, American Welding Society 1989.
- [27] ASM Handbook, Vol. 6, Welding, Brazing and Soldering 1995.
- [28] Maji B, Krishnan M. The effect of microstructure on the shape recovery of a Fe–Mn–Si–Cr–Ni stainless steel shape memory alloy. *Scripta Mater* 2003;48:71–7.
- [29] Stanford N, Dunne D, Monaghan B. Austenite stability in Fe–Mn–Si-based shape memory alloys. *J. Alloys Compd* 2007;430:107–15.
- [30] Wen Y, Peng H, Sun P, Liu G, Li N. A novel training-free cast Fe–18Mn–5.5Si–9.5Cr–4Ni shape memory alloy with lathy delta ferrite. *Scripta Mater* 2010;62:55–8.
- [31] Maji B, Krishnan M, Rama M. The microstructure of an Fe–Mn–Si–Cr–Ni stainless steel shape memory alloy. *Metall Mater Trans A* 2003;34:1029.
- [32] Bu D, Peng H, Wen Y, Li N. Influence of ageing on wear resistance of an Fe–Mn–Si–Cr–Ni–Ti–C shape memory alloy. *Mater Des* 2011;32:2969–73.
- [33] Ackerbauer S, Krendelsberger N, Weitzer F, Hiebl K, Schuster J. The constitution of the ternary system Fe–Ni–Si. *Intermetall* 2009;17:414–20.
- [34] Jiang BH, Sun L, Li R, Hsu TY. Influence of austenite grain size on $\gamma \leftrightarrow \epsilon$ martensitic transformation temperature in Fe–Mn–Si–Cr alloys. *Scr Metall Mater* 1995;33:63–8.
- [35] ASM Handbook, Vol. 14, Forming and Forging 1995.
- [36] Numerical System, Chemical composition. SAE J403 MAY94. SAE Handbook 1995; 1:3.01. Society of Automotive Engineers. Warrendale, U.S.A.
- [37] ISO system of limits and fits. Bases of tolerances, deviations and fits. ISO R286 1:88. International Organization for Standardization. Bruxelles 1993.
- [38] Preferred Limits and Fits for Cylindrical Parts. ANSI Standard B4.1-1967 (confirmed in 1979). American Society of Mechanical Engineers. New York.